

Non-linear anomalous Edelstein response at altermagnetic interfaces

Mattia Trama,^{1,2,*} Irene Gaiardoni,³ Claudio Guarcello,^{3,4} Jorge I. Facio,⁵ Alfonso Maiellaro,^{3,6} Francesco Romeo,^{3,4} Roberta Citro,^{3,6,4,†} and Jeroen van den Brink^{1,2}

¹*Institute for Theoretical Solid State Physics, IFW Dresden, Helmholtzstr. 20, 01069 Dresden, Germany*

²*Würzburg-Dresden Cluster of Excellence ct.qmat, Helmholtzstrasse 20, 01069 Dresden, Germany*

³*Physics Department “E.R. Caianiello”, Università degli studi di*

Salerno, Via Giovanni Paolo II, 132, I-84084 Fisciano (Sa), Italy

⁴*INFN - Sezione collegata di Salerno, Complesso Univ. Monte S. Angelo, I-80126 Napoli, Italy*

⁵*Centro Atómico Bariloche, Instituto de Nanociencia y Nanotecnología (CNEA-CONICET) and Instituto Balseiro, Av. Bustillo, 9500, Argentina*

⁶*CNR-SPIN, I-84084 Fisciano (Salerno), Italy, c/o Università di Salerno, I-84084 Fisciano (Salerno), Italy*

In altermagnets, time-reversal symmetry breaking spin-polarizes electronic states, while total magnetization remains zero. In addition, at altermagnetic surfaces Rashba-spin orbit coupling is activated due to broken inversion symmetry, introducing a competing spin-momentum locking interaction. Here we show that their interplay leads to the formation of complex, chiral spin textures that offer novel, non-linear spin-to-charge conversion properties. Whereas altermagnetic order suppresses the canonical linear in-plane Rashba-Edelstein response, we establish the presence of an *anomalous* transverse Edelstein effect for planar applied electric and magnetic field, or alternatively, an in-plane magnetization. Moreover the non-linear Edelstein response resulting purely from electric fields also triggers the anomalous out-of-plane magnetization. We determine the anomalous response with a model based on the ab-initio electronic structure of RuO₂ bilayers, ultimately opening experimental avenues to explore spin-charge conversion phenomena at altermagnetic interfaces.

Altermagnets (AMs) are a class of magnetic materials with a total magnetization that vanishes by symmetry while at the same time Kramers’ degeneracy is lifted [1–11]. Unlike antiferromagnets, for which the vanishing of the magnetization is enforced by the combined action of time-reversal and translation/inversion symmetry, in AMs this involves an additional rotation or mirror operation. This symmetry operation causes the band structure to be spin-polarized, also in the absence of spin-orbit coupling (SOC) [1]. The presence of spin-polarized bands and Fermi surfaces makes AMs potentially appealing as spin-polarized current sources for antiferromagnetic spintronics [5, 12–16]. On the basis of magnetic symmetries [1], an extensive set of candidate materials exhibiting collinear altermagnetism have been identified from electronic structure calculations, both 3D [8] and 2D [17]. While experimentally the spin-splitting of electronic bands has been observed by photoemission spectroscopy [18–22], exploration of AM (magneto-) transport properties for antiferromagnetic spintronic purposes, which capitalizes on their strong exchange interactions [23], has only just begun and has so far focused on harnessing their anomalous and spin Hall effects [9, 13, 15, 19, 24–27]. For instance it has recently been shown that altermagnetic spin-splitting is at the origin of a spin Hall effect in RuO₂ [12].

In this context, we identify natural possibilities for spin-to-charge conversion processes at AM interfaces that fundamentally go beyond the canonical linear Rashba-Edelstein effect [28–30], where a surface electric current

produces an in-plane magnetization that, as we will show, is actually suppressed by AM. Instead, the competition between Rashba SOC (RSOC) and AM triggers *anomalous* non-linear Edelstein effects (EEs): we will show that a magnetization transverse to the interface is induced by an in-plane applied electric and magnetic field (or an in-plane magnetization) – or alternatively as non-linear magnetic response to purely planar electric fields. This spin-to-charge conversion in electric and magnetic field

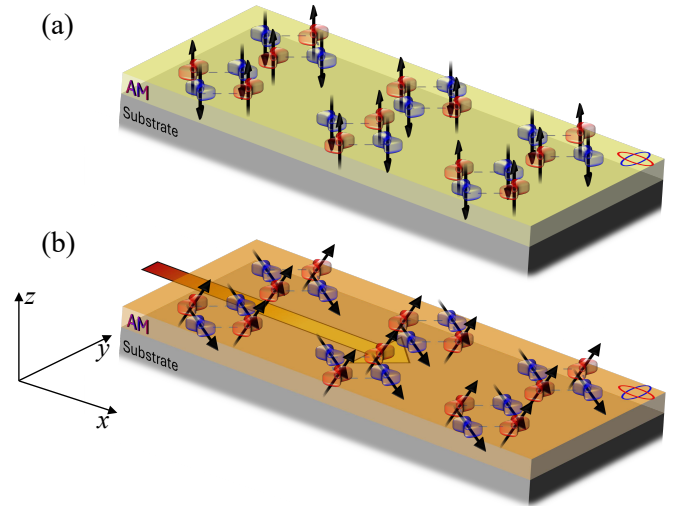


Figure 1. Schematic representation of the transversal, non-linear altermagnetic EE. (a) Out-of-plane spin arrangement in the absence of driving current with zero net magnetization and (b) homogeneous tilting of the out-of-plane spins due to an in-plane driving current that generates a transverse magnetic field.

* m.trama@ifw-dresden.de

† rocitro@unisa.it

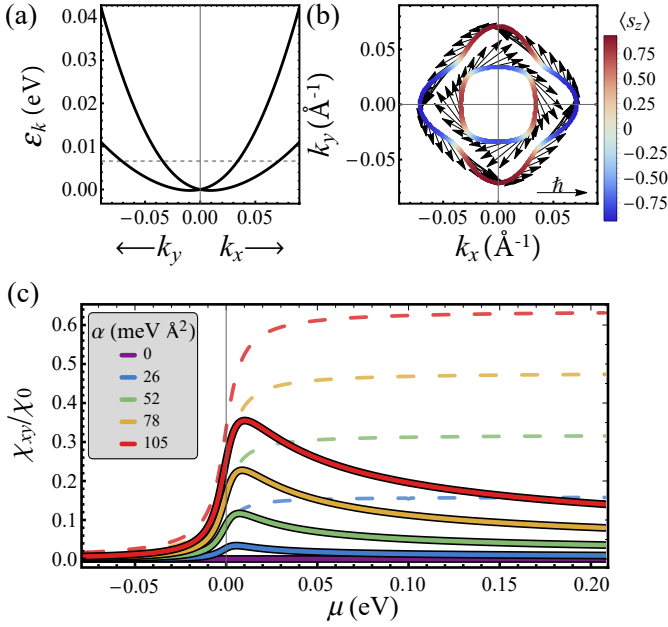


Figure 2. **Competing altermagnetic and Rashba spin-orbit interactions.** (a) Electronic dispersion resulting from the continuum Hamiltonian (1) $\alpha = 52 \text{ meV } \text{\AA}$. (b) Fermi surface and spin structure for fixed chemical potential (dashed line in panel (a)). (c) linear Edelstein susceptibility χ_{xy}/χ_0 ($\chi_0 = 2.44 \times 10^2 \mu_B \text{\AA} \text{ V}^{-1}$) for different α . The dashed lines correspond to the pure RSOC case ($\gamma = 0$).

can be depicted by an in-plane current forcing the magnetic moments out of the plane, as schematically indicated in Fig. 1. Also the purely electric non-linear case will be understood in such basic terms.

It should be noted that, while AM may be strictly defined in the limit of vanishing SOC, it still defines an essential energy scale, determining for instance the altermagnetic anomalous Hall response [9] and electronic properties related to the topology of altermagnetic electronic structures [24]. At interfaces and in 2D, the RSOC is induced by inversion-symmetry breaking and naturally produces a spin-momentum locking without net magnetization. Indeed, the coexistence of AM spin splitting and the RSOC has been pointed out [31, 32], but so far not investigated as a mechanism to achieve an anomalous Rashba-Edelstein response and non-linear spin-to-charge conversion.

The standard linear EE originating from RSOC locks the spin of electrons in-plane and orthogonal to their momentum, respecting spinfull time-reversal symmetry. Then, an applied in-plane electric field results in an imbalance in the spin density at the Fermi surface and a net in-plane magnetization orthogonal to the induced current. Interestingly, in the presence of only RSOC, the second-order non-linear EE [33–35] vanishes by symmetry. However, it may be triggered by, for instance, introducing orbital degrees of freedom [33] or a time-dependent setting [34]. In contrast to RSOC, AM breaks

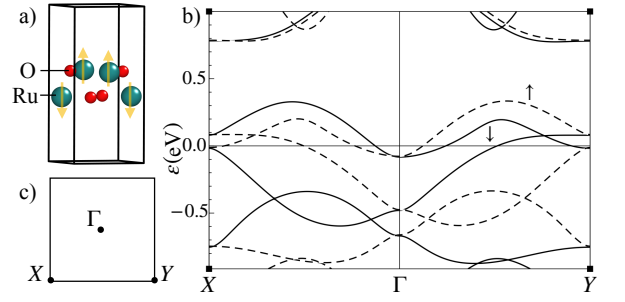


Figure 3. **Bilayer of RuO_2 and its electronic structure density-functional calculations.** (a) Crystal structure. (b) Band structure along high symmetry points indicated in (c).

time-reversal symmetry, so that in collinear AMs opposite momenta carry the same spin orientation. This renders the momentum-space magnetic textures generated by RSOC and AM fundamentally different: the two interactions compete.

Altermagnetic Rashba model — To explore the physical consequences of this competition, we start by considering the 2D effective continuum Hamiltonian

$$\hat{H} = \frac{k^2}{2m} + \gamma(k_x^2 - k_y^2)\hat{\sigma}_z + \alpha\hat{z} \cdot (\vec{\sigma} \times \mathbf{k}) - \mu, \quad (1)$$

where $\hat{\sigma}_i$ is the Pauli matrix in the direction \hat{i} , α is the RSOC interaction, γ is the altermagnetic d -wave coupling with symmetry $[C_2||C_{4z}]$ [1], μ is the chemical potential, and \hbar is set to unity. The resulting bands and their spin-texture for given chemical potential are illustrated in Fig. 2(a,b). Note that the chirality of the resulting non-coplanar spin texture is determined by $\text{sgn}(\gamma\alpha)$.

To keep contact with real materials, we consider a bilayer of RuO_2 and estimate its altermagnetic coupling γ . We note that the magnetic nature of RuO_2 is in itself an interesting debated question [36–40]. Here, we consider this system just as a d -wave altermagnetic model in which it is in principle possible to engineer via gating both the band filling and effective RSOC. Based on the bulk crystal structure, we construct a bilayer oriented along the c -axis of RuO_2 bulk, containing two Ru ions related by fourfold rotoinversion symmetry. The altermagnetic bilayer can be represented with the space group Cmm2 (No. 35), with a unit cell having $a = 6.35 \text{ \AA}$. For this structure, we perform density-functional calculations in the generalized gradient approximation based on the FPLO code [41]. We use a k -points mesh having $16 \times 16 \times 1$ subdivisions along with a tetrahedron method for Brillouin zone integrations. Figure 3 shows the band structure in the absence of RSOC. We apply our effective two-band model to describe the two bands nearest to the Fermi energy at Γ . From a fit of Eq. (1) to these bands, we obtain $m = 0.152 \text{ eV}^{-1} \text{\AA}^{-2}$ and $\gamma = 1.881 \text{ eV } \text{\AA}^2$ (see Appendix B).

Linear Edelstein responses — The linear EE is defined through $\langle \sigma_j \rangle = \chi_{ij} E_i$, where E_i is the electric field along

the direction \hat{i} and χ_{ij} is the Edelstein susceptibility. The spin accumulation $\langle \sigma_j \rangle$ can be obtained in the Boltzmann framework as

$$\langle \sigma_j \rangle (\mu) = -\mu_b \sum_{\mathbf{k}, \nu} |e| \left(\tilde{\Lambda}_{\mathbf{k}}^{\nu} \cdot \mathbf{E} \right) \delta[\varepsilon_{\mathbf{k}}^{\nu} - \mu] (\nu s_j(\mathbf{k})), \quad (2)$$

where we made μ explicit in the Dirac delta since we treat it as an external parameter, μ_b is the Bohr magneton, $\varepsilon_{\mathbf{k}}$ are the eigenvalues with band index $\nu = \pm$ that, for the Hamiltonian in Eq. (1), are given by

$$\varepsilon_{\mathbf{k}}^{\pm} = \frac{k^2}{2m} \pm \sqrt{\alpha^2(k_y^2 + k_x^2) + \gamma^2(k_x^2 - k_y^2)^2} = \frac{k^2}{2m} \pm \delta\varepsilon, \quad (3)$$

and s_j is the j -component of the spin vector $\mathbf{s} = (\alpha k_y, -\alpha k_x, \gamma(k_x^2 - k_y^2)) / \delta\varepsilon$. The mean free path is computed within the relaxation-time approximation, $\tilde{\Lambda}_{\mathbf{k}}^{\nu} = \tau_{\mathbf{k}}^{\nu} \mathbf{v}_{\mathbf{k}}^{\nu}$, with $\tau_{\mathbf{k}}^{\nu}$ and $\mathbf{v}_{\mathbf{k}}^{\nu} = \nabla_{\mathbf{k}} \varepsilon_{\mathbf{k}}^{\nu}$ being the transport lifetime and the group velocity, respectively.

Supposing, for simplicity, that $\tau_{\mathbf{k}}^{\nu} = \tau$, and taking $\mathbf{E} = E_0 \hat{x}$, Eq. (2) can be written in terms of the susceptibility per unit cell, χ_{xi} , as

$$\chi_{xj} = -\chi_0 \sum_{\nu=\pm} \int d^2\mathbf{k} \nu s_j(\mathbf{k}) \delta(\varepsilon_{\mathbf{k}}^{\nu} - \mu) v_x^{\nu}(\mathbf{k}), \quad (4)$$

where $\chi_0 = \frac{\tau |e| \mu_b S_{\text{cell}}}{4\pi^2 a}$, with a being the lattice parameter, S_{cell} the area of the unit cell, and $\tau = 10^{-12}$ s the typical order of magnitude of oxides [29].

The conventional EE is governed by χ_{xy} and certainly RSOC alone is sufficient to induce it, as shown for our continuum Hamiltonian in Fig 2(c). Without AM and in-plane magnetic field ($\gamma = 0$), the linear Edelstein susceptibility χ_{xy} scales with the RSOC α , and quickly saturates for large chemical potential μ , see dashed lines in Fig 2(c). Here, we vary α in a range around 0.05 eV Å which is a realistic range of values for oxides [42–45], and may be experimentally achieved by, e.g., a tunable top-gate or interfacial electric field [46]. Clearly, a finite altermagnetic coupling, γ , significantly suppresses the EE, particularly at higher μ , and this for any value of γ leads to a pronounced peak in χ_{xy} in the vicinity of the band bottom. Thus, as we expected on the basis of symmetry considerations, AM and the conventional EE strongly compete.

Definition of non-linear Edelstein responses — Clearly, the RSOC, with its in-plane spin-momentum locking, cannot alone produce an out-of-plane, transverse Edelstein response, i.e., χ_{xz} vanishes identically. Even if the γ term tends to align spins out-of-plane, RSOC in the presence of altermagnetism is not sufficient to induce a transversal response. Since $\varepsilon_{\mathbf{k}}^{\pm} = \varepsilon_{-\mathbf{k}}^{\pm}$, while $v_x^{\pm}(\mathbf{k}) = -v_x^{\pm}(-\mathbf{k})$, the component χ_{xz} is seen to vanish being $s_z(-\mathbf{k}) = s_z(\mathbf{k})$. Such an anomalous transversal response actually requires altermagnetism and a non-linear EE, as we will detail in the following. Indeed, the presence of an additional (effective) *in-plane* magnetic field breaks the $\mathbf{k} \rightarrow -\mathbf{k}$ symmetry, thus allowing

out-of-plane Edelstein responses. One may distinguish two types of non-linear response, one involving an in-plane electric and magnetic field and one involving only in-plane electric fields, but up to second order (see Appendix A).

The case of combined electric and magnetic fields is most easily considered by introducing a Zeeman term in Eq. (1), orthogonal to the applied electric field E_x , of the form $H_h = h_y \sigma_y$ and then using Eq. (4). The H_h term corresponds to an effective homogeneous spin splitting, which may arise from a Zeeman field or from weak ferromagnetism induced by Dzyaloshinskii–Moriya (DM) interactions, generally allowed by AM symmetries [17, 47–49]. This response is nonlinear as it depends both linearly on electric field *and* magnetic coupling and vanishes when either one is zero (see Appendix C). Incorporating \mathbf{h} directly into the Hamiltonian offers the advantage that it is easy to go beyond its linear response.

To assess the non-linear EE involving only electric fields, it is more convenient to introduce the second order Edelstein susceptibility of the form $\langle \sigma_z \rangle = \tilde{\chi}_{xxz} E_x^2$, with

$$\tilde{\chi}_{xxz} = -\tilde{\chi}_0 \sum_{\nu=\pm} \int d^2\mathbf{k} \nu \frac{\partial s_z(\mathbf{k})}{\partial k_x} \delta(\varepsilon_{\mathbf{k}}^{\nu} - \mu) v_x^{\nu}(\mathbf{k}), \quad (5)$$

where $\tilde{\chi}_0 = \frac{\mu_B e^2 \tau^2}{4\pi^2} S_{\text{cell}}$ (see Appendix D for the full derivation). In this case, the symmetry argument discussed above shows that the integrand function is even rather than odd, since $\partial_{k_x} s_z(\mathbf{k}) = -\partial_{k_x} s_z(-\mathbf{k})$. Therefore, there are no symmetries that force the response to vanish.

Calculation of non-linear Edelstein responses — Having established that, due to the interplay of RSOC with AM symmetry allows anomalous non-linear EEs, we now determine them in an experimentally relevant parameter range. For the effective in-plane field h_y resulting from weak ferromagnetism, we choose $h_y = 40$ meV as benchmark value [17]. The first effect of the in-plane Zeeman coupling is to lift the degeneracy at Γ , as shown in Fig. 4(a), in contrast with the simple Rashba system, for which the in-plane magnetic field can only move the degeneracy point. Moreover, as mentioned above, it breaks the symmetry of the system both in the shape of the Fermi surface and in the chiral structure of the spin, as one can see in Fig. 4(b). The resulting Edelstein susceptibility tensor χ is shown in Fig. 4(c). While χ_{xx} vanishes, χ_{xy} depends non-monotonically on chemical potential and reaches its maximum after occupying the first band. Compared to the case $h_y = 0$, χ_{xy} grows slower to its maximum, but reaches a value similar to the situation with pure RSOC. Moreover, the in-plane magnetic field is able to induce a substantial out-of-plane anomalous transversal response χ_{xz} due to the large altermagnetic coupling, with the transversal component reaching larger values than the in-plane response, even larger than the canonical linear RSOC situation.

The non-monotonic behaviour of χ_{xz} as a function of μ derives from the competition and complex interplay

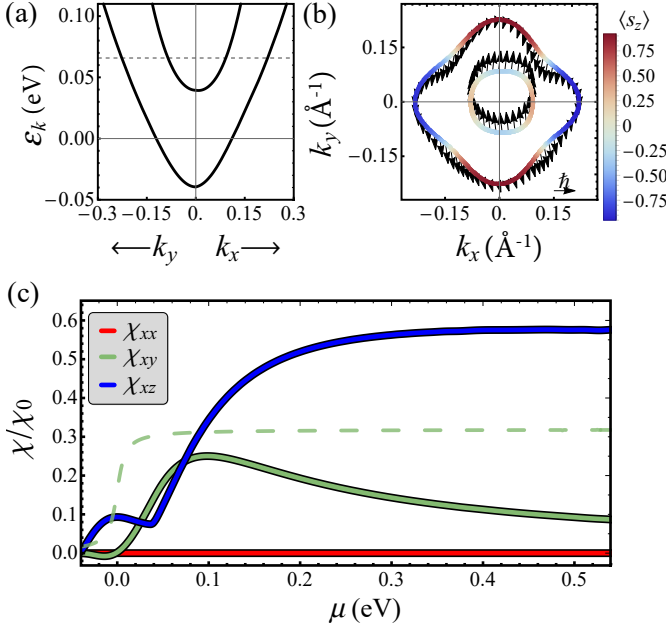


Figure 4. **Anomalous non-linear EE due to a combined planar magnetic and electric field.** (a) Electronic dispersion from Hamiltonian (1) with $\alpha = 52$ meV Å and $h_y = 40$ meV. (b) Fermi surface and spin structure for fixed chemical potential, see the dashed line in (a). (c) Edelstein response χ_{xi}/χ_0 ($\chi_0 = 2.44 \times 10^2 \mu_B \text{ Å V}^{-1}$) for the directions $i = x, y, z$. The green dashed line corresponds to the pure RSOC case ($\gamma = h_y = 0$).

of the different interactions. At low filling, even an infinitesimal h_y breaks the $\mathbf{k} \rightarrow -\mathbf{k}$ symmetry in the integrand in Eq. (4), leading to a characteristic threshold behavior in the response. Increasing μ , the out-of-plane response is first slightly suppressed and later saturates to a constant value in the altermagnetic-dominated regime. Crucially, all three ingredients are required to exhibit the out-of-plane response: the altermagnetic interaction enforces an out-of-plane magnetization, the weak ferromagnetism breaks its otherwise symmetric pattern, and the RSOC induces the spin-momentum locking required for this non-linear Edelstein response.

On the other hand, without inducing any modification to the energy spectrum, i.e., the electronic bands and the spin structure correspond to the one shown in Fig. 2, an out-of-plane, second-order EE is obtained. The computed Edelstein susceptibilities from Eq. (5), for different values of the RSOC, are shown in Fig. 5. One observes a signature peak right above the band crossing at $\varepsilon = 0$, which decreases with the increasing of α , and then a steady decrease of $\tilde{\chi}_{xxz}$ for larger μ . This anomalous response is characteristic of altermagnetic systems with RSOC and vanishes for either $\alpha = 0$ or $\gamma = 0$ (see Appendix D for details). Therefore, this non-monotonic behaviour allows to individuate the location of band crossing due to RSOC and the strength of the coupling in altermagnetic surfaces. A detailed analysis is presented in

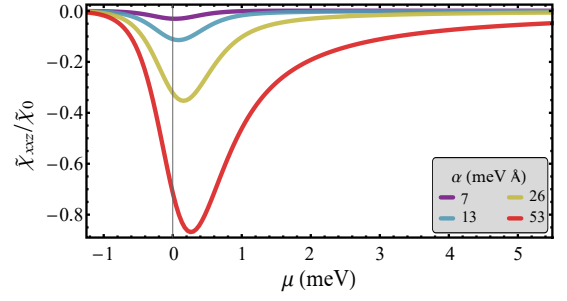


Figure 5. **Second-order electric Edelstein response.** $\tilde{\chi}_{xxz}/\tilde{\chi}_0$ (with $\tilde{\chi}_0 = 2.36 \times 10^6 \text{ Å}^2 \text{ V}^{-2}$) versus μ for different values of α .

Appendix C. When generalized to finite frequencies, the non-linear susceptibility $\tilde{\chi}_{xxz}$ induces second-harmonic generation. This, in principle, offers an experimentally attractive route to detect such a non-linear response. In our case, the rectifying and doubled frequency terms $\langle \tilde{\chi}_{xxz} \rangle = \text{Re}[\langle \tilde{\chi}_{xxz}^0 \rangle + \langle \tilde{\chi}_{xxz}^{2\omega} \rangle e^{2i\omega t}]$ appear, which are related to Eq. (5) as $\langle \tilde{\chi}_{xxz}^0 \rangle = \tilde{\chi}_{xxz}/2(1 + i\omega\tau)$ and $\langle \tilde{\chi}_{xxz}^{2\omega} \rangle = \tilde{\chi}_{xxz}/2(1 + i\omega\tau)(1 + 2i\omega\tau)$.

Summary and outlook — Using a continuum description for AMs based on ab-initio electronic band structure calculations, we have shown that the interplay of altermagnetic coupling with an interfacial RSOC gives rise to the appearance of out-of-plane spin polarizations throughout the Brillouin zone via non-linear EEs. While the in-plane linear response can be strongly suppressed with the band filling, the non-linear Edelstein susceptibilities exhibit strong non-monotonic behaviour. The non-linear responses we determined involve a term that depends on the in-plane electric and the magnetic fields, and a second-order term in the electric field. For the former term, an anomalous out-of-plane magnetization is generated, exceeding the in-plane EE. For the latter term, the transverse magnetization is the only response allowed, and it is enhanced when the chemical potential is close to the crossing of the electronic bands due to RSOC. In both cases, it is remarkable that out-of-plane magnetization is obtained in response only to in-plane fields. All these features can be exploited to fully characterize the altermagnetic nature of the electron gas at the interface. Indeed, the behaviour of the magnetization with the filling can be directly related to the presence of the spin-orbit, DM interaction and band crossings. On the other hand, the uncovered *anomalous* non-linear altermagnetic Edelstein responses may be used experimentally to induce efficient spin-to-charge conversion at altermagnetic interfaces leading to novel electronic and spintronic applications.

Acknowledgments — We thank Oleg Janson and Carmine Autieri for fruitful discussions. We thank Ulrike Nitzsche for technical assistance. M.T. acknowledges financial support from “Fondazione Angelo Della Riccia”. This work was financed by Horizon Eu-

rope EIC Pathfinder under the grant IQARO number 101115190. R.C. and F.R. acknowledge funding from Ministero dell'Istruzione, dell'Università e della Ricerca (MIUR) for the PRIN project QUESTIONS (Grant No. PRIN P2022KWFBBH) and STIMO (Grant No. PRIN 2022TWZ9NR). This work received support from the PNRR MUR project PE0000023-NQSTI (TOPQIN and SPUNTO). This work was supported by the Deutsche Forschungsgemeinschaft (DFG, German Research Foundation) through the Sonderforschungsbereich SFB 1143, Grant No. YE 232/2-1, and under Germany's Excellence

Strategy through the Würzburg-Dresden Cluster of Excellence on Complexity and Topology in Quantum Matter – ct.qmat (EXC 2147, Project IDs No. 390858490 and No. 392019).

Contributions — R.C., M.T., I.G. and J.v.d.B. conceived the ideas and designed the research; M.T., I.G. and C.G. performed the transport calculations; J.I.F. performed DFT calculations; all the authors interpreted and analyzed the results; M.T., C.G. R.C., J.I.F. and J.v.d.B. wrote the first version of the manuscript with input from all authors; all the authors reviewed the manuscript; R.C. and J.v.d.B. supervised the study.

-
- [1] L. Šmejkal, J. Sinova, and T. Jungwirth, *Phys. Rev. X* **12**, 031042 (2022).
 - [2] I. I. Mazin, K. Koepf, M. D. Johannes, R. González-Hernández, and L. Šmejkal, *Proceedings of the National Academy of Sciences* **118**, e2108924118 (2021).
 - [3] S. Hayami, Y. Yanagi, and H. Kusunose, *Journal of the Physical Society of Japan* **88**, 123702 (2019).
 - [4] L. Šmejkal, R. González-Hernández, T. Jungwirth, and J. Sinova, *Science Advances* **6**, eaaz8809 (2020).
 - [5] M. Naka, S. Hayami, H. Kusunose, Y. Yanagi, Y. Motome, and H. Seo, *Nature Communications* **10**, 4305 (2019).
 - [6] L.-D. Yuan, Z. Wang, J.-W. Luo, E. I. Rashba, and A. Zunger, *Phys. Rev. B* **102**, 014422 (2020).
 - [7] M. Naka, Y. Motome, and H. Seo, *Phys. Rev. B* **103**, 125114 (2021).
 - [8] Y. Guo, H. Liu, O. Janson, I. C. Fulga, J. van den Brink, and J. I. Facio, *Materials Today Physics* **32**, 100991 (2023).
 - [9] T. Sato, S. Haddad, I. C. Fulga, F. F. Assaad, and J. van den Brink, *Phys. Rev. Lett.* **133**, 086503 (2024).
 - [10] L. Šmejkal, A. H. MacDonald, J. Sinova, S. Nakatsuji, and T. Jungwirth, *Nature Reviews Materials* **7**, 482 (2022).
 - [11] H.-Y. Ma, M. Hu, N. Li, J. Liu, W. Yao, J.-F. Jia, and J. Liu, *Nature Communications* **12**, 2846 (2021).
 - [12] H. Bai, Y. C. Zhang, Y. J. Zhou, P. Chen, C. H. Wan, L. Han, W. X. Zhu, S. X. Liang, Y. C. Su, X. F. Han, F. Pan, and C. Song, *Phys. Rev. Lett.* **130**, 216701 (2023).
 - [13] R. González-Hernández, L. Šmejkal, K. Výborný, Y. Yahagi, J. Sinova, T. c. v. Jungwirth, and J. Železný, *Phys. Rev. Lett.* **126**, 127701 (2021).
 - [14] J. Železný, H. Gao, A. Manchon, F. Freimuth, Y. Mokrousov, J. Zemen, J. Mašek, J. Sinova, and T. Jungwirth, *Phys. Rev. B* **95**, 014403 (2017).
 - [15] H. Bai, L. Han, X. Y. Feng, Y. J. Zhou, R. X. Su, Q. Wang, L. Y. Liao, W. X. Zhu, X. Z. Chen, F. Pan, X. L. Fan, and C. Song, *Phys. Rev. Lett.* **128**, 197202 (2022).
 - [16] A. Bose, N. J. Schreiber, R. Jain, D.-F. Shao, H. P. Nair, J. Sun, X. S. Zhang, D. A. Muller, E. Y. Tsybal, D. G. Schlom, and D. C. Ralph, *Nature Electronics* **5**, 267 (2022).
 - [17] M. Milivojević, M. Orozović, S. Picozzi, M. Gmitra, and S. Stavič, *2D Materials* **11**, 035025 (2024).
 - [18] M. Zeng, M.-Y. Zhu, Y.-P. Zhu, X.-R. Liu, X.-M. Ma, Y.-J. Hao, P. Liu, G. Qu, Y. Yang, Z. Jiang, K. Yamagami, M. Arita, X. Zhang, T.-H. Shao, Y. Dai, K. Shimada, Z. Liu, M. Ye, Y. Huang, Q. Liu, and C. Liu, *Advanced Science*, 2406529 (2024).
 - [19] S. Reimers, L. Odenbreit, L. Šmejkal, V. N. Strocov, P. Constantinou, A. B. Hellenes, R. Jaeschke Ubierno, W. H. Campos, V. K. Bharadwaj, A. Chakraborty, T. Denneulin, W. Shi, R. E. Dunin-Borkowski, S. Das, M. Kläui, J. Sinova, and M. Jourdan, *Nature Communications* **15**, 2116 (2024).
 - [20] W. Lu, S. Feng, Y. Wang, D. Chen, Z. Lin, X. Liang, S. Liu, W. Feng, K. Yamagami, J. Liu, et al., *arXiv preprint arXiv:2407.13497* (2024), 10.48550/arXiv.2407.13497.
 - [21] B. Jiang, M. Hu, J. Bai, Z. Song, C. Mu, G. Qu, W. Li, W. Zhu, H. Pi, Z. Wei, Y. Sun, Y. Huang, X. Zheng, Y. Peng, L. He, S. Li, J. Luo, Z. Li, G. Chen, H. Li, H. Weng, and T. Qian, (2024), *arXiv:2408.00320 [cond-mat.mtrl-sci]*.
 - [22] F. Zhang, X. Cheng, Z. Yin, C. Liu, L. Deng, Y. Qiao, Z. Shi, S. Zhang, J. Lin, Z. Liu, M. Ye, Y. Huang, X. Meng, C. Zhang, T. Okuda, K. Shimada, S. Cui, Y. Zhao, G.-H. Cao, S. Qiao, J. Liu, and C. Chen, (2024), *arXiv:2407.19555 [cond-mat.str-el]*.
 - [23] A. Dal Din, O. J. Amin, P. Wadley, and K. W. Edmonds, *npj Spintronics* **2**, 25 (2024).
 - [24] C. Li, M. Hu, Z. Li, Y. Wang, W. Chen, B. Thiragarajan, M. Leandersson, C. Polley, T. Kim, H. Liu, C. Fulga, M. G. Vergniory, O. Janson, O. Tjénberg, and J. van den Brink, *arXiv preprint arXiv:2405.14777* (2024), 10.48550/arXiv.2405.14777.
 - [25] Z. Feng, X. Zhou, L. Šmejkal, L. Wu, Z. Zhu, H. Guo, R. González-Hernández, X. Wang, H. Yan, P. Qin, X. Zhang, H. Wu, H. Chen, Z. Meng, L. Liu, Z. Xia, J. Sinova, T. Jungwirth, and Z. Liu, *Nature Electronics* **5**, 735 (2022).
 - [26] R. D. Gonzalez Betancourt, J. Zubáć, R. Gonzalez-Hernandez, K. Geishendorf, Z. Šobáň, G. Springholz, K. Olejník, L. Šmejkal, J. Sinova, T. Jungwirth, S. T. B. Goennenwein, A. Thomas, H. Reichlová, J. Železný, and D. Kriegner, *Phys. Rev. Lett.* **130**, 036702 (2023).
 - [27] M. Hu, O. Janson, C. Felser, P. McClarty, J. van den Brink, and M. G. Vergniory, (2024), *arXiv:2410.17993 [cond-mat.mtrl-sci]*.
 - [28] V. M. Edelstein, *Solid State Communications* **73**, 233

- (1990).
- [29] M. Trama, V. Cataudella, C. A. Perroni, F. Romeo, and R. Citro, *Nanomaterials* **12** (2022), 10.3390/nano12142494.
 - [30] M. Trama, *Il Nuovo Cimento C* **100**, 47 (2024).
 - [31] C. Sun and J. Linder, *Phys. Rev. B* **108**, L140408 (2023).
 - [32] M. Amundsen, A. Brataas, and J. Linder, *Phys. Rev. B* **110**, 054427 (2024).
 - [33] I. Baek, S. Han, S. Cheon, and H.-W. Lee, *npj Spintronics* **2**, 33 (2024).
 - [34] G. Vignale and I. V. Tokatly, *Phys. Rev. B* **93**, 035310 (2016).
 - [35] H. Xu, J. Zhou, H. Wang, and J. Li, *Phys. Rev. B* **103**, 205417 (2021).
 - [36] Z. Lin, D. Chen, W. Lu, X. Liang, S. Feng, K. Yamagami, J. Osiecki, M. Leandersson, B. Thiagarajan, J. Liu, C. Felser, and J. Ma, (2024), [arXiv:2402.04995 \[cond-mat.mtrl-sci\]](#).
 - [37] J. Liu, J. Zhan, T. Li, J. Liu, S. Cheng, Y. Shi, L. Deng, M. Zhang, C. Li, J. Ding, Q. Jiang, M. Ye, Z. Liu, Z. Jiang, S. Wang, Q. Li, Y. Xie, Y. Wang, S. Qiao, J. Wen, Y. Sun, and D. Shen, (2024), 10.48550/arXiv.2409.13504.
 - [38] S. G. Jeong, I. H. Choi, S. Nair, L. Buiarelli, B. Pourbahari, J. Y. Oh, N. Bassim, A. Seo, W. S. Choi, R. M. Fernandes, *et al.*, [arXiv preprint arXiv:2405.05838](#) (2024), 10.48550/arXiv.2405.05838.
 - [39] L. Kiefer, F. Wirth, A. Bertin, P. Becker, L. Bohatý, K. Schmalzl, A. Stunault, J. A. Rodríguez-Velamazán, O. Fabelo, and M. Braden, [arXiv preprint arXiv:2410.05850](#) (2024), 10.48550/arXiv.2410.05850.
 - [40] M. Wenzel, E. Uykur, S. Röckler, M. Schmidt, O. Janson, A. Tiwari, M. Dressel, and A. A. Tsirlin, [arXiv preprint arXiv:2407.11148](#) (2024), 10.48550/arXiv.2407.11148.
 - [41] K. Koepernik and H. Eschrig, *Phys. Rev. B* **59**, 1743 (1999).
 - [42] E. Lesne, Y. Fu, S. Oyarzun, J. C. Rojas-Sánchez, D. C. Vaz, H. Naganuma, G. Sicoli, J. P. Attané, M. Jamet, E. Jacquet, J. M. George, A. Barthélémy, H. Jaffrès, A. Fert, M. Bibes, and L. Vila, *Nature Materials* **15**, 1261 (2016).
 - [43] M. Trama, V. Cataudella, C. A. Perroni, F. Romeo, and R. Citro, *Phys. Rev. B* **106**, 075430 (2022).
 - [44] M. Trama, V. Cataudella, and C. A. Perroni, *Phys. Rev. Res.* **3**, 043038 (2021).
 - [45] J. Zhai, M. Trama, H. Liu, Z. Zhu, Y. Zhu, C. A. Perroni, R. Citro, P. He, and J. Shen, *Nano Letters* **23**, 11892 (2023).
 - [46] A. D. Caviglia, M. Gabay, S. Gariglio, N. Reyren, C. Cancellieri, and J.-M. Triscone, *Phys. Rev. Lett.* **104**, 126803 (2010).
 - [47] N. Wang, J. Chen, N. Ding, H. Zhang, S. Dong, and S.-S. Wang, *Phys. Rev. B* **106**, 064435 (2022).
 - [48] S.-W. Cheong and F.-T. Huang, *npj Quantum Materials* **9**, 13 (2024).
 - [49] C. Autieri, R. M. Sattigeri, G. Cuono, and A. Fakhredine, (2024), [arXiv:2312.07678 \[cond-mat.mtrl-sci\]](#).

Appendix A: Scaling in the electric and magnetic field

The effect of RSOC and the magnetic field to the altermagnetic system, can be understood on the basis of a heuristic argument based on the accumulated spin considering only four points of the Fermi surface. The Fermi surface generated from the pure altermagnetic Hamiltonian is

$$H = \frac{k^2}{2m} + \gamma(k_x^2 - k_y^2)\sigma_z, \quad (\text{A1})$$

which has the form of two spin-polarized orthogonal ellipses centered around Γ . Let us consider the four points at the end of the major axis of the ellipses in the momentum space $\pm K_x = (\pm K, 0)$ and $\pm K_y = (0, \pm K)$, where K is a large enough quasi-momentum, such as $\gamma K \gg \alpha$ and $\gamma K^2 \gg h_y$, where α and h_y are the RSOC parameter and the magnetic Zeeman field that will act as a perturbation. Let us consider the perturbation due to

the RSOC and the magnetic field

$$V = \alpha(k_y\sigma_x - k_x\sigma_y) + h_y\sigma_y, \quad (\text{A2})$$

the spin along z is therefore

$$s_z = \frac{\gamma(k_x^2 - k_y^2)}{\sqrt{\gamma^2(k_x^2 - k_y^2)^2 + \alpha^2(-k_x + h_y)^2 + \alpha^2 k_y^2}}. \quad (\text{A3})$$

We consider the electric field applied to the system by taking into account the shift in the momentum δk due to the equation of motion, i.e., $E_x = \frac{\tau \delta k}{e}$, where τ is the characteristic scattering time of the system. Therefore, the total spin along z is

$$S_z = s_z(K + \delta k, 0) + s_z(-K + \delta k, 0) + s_z(\delta k, K) + s_z(\delta k, -K), \quad (\text{A4})$$

which we expand to first order in h_y and to second order in δk , so that

$$S_z = \frac{3\alpha^4\gamma K^4}{(K^2(\alpha^2 + \gamma^2 K^2))^{5/2}}\delta k^2 - \frac{2(\alpha^2\gamma(\alpha^2 + 4\gamma^2 K^2))}{K(\alpha^2 + \gamma^2 K^2)^{5/2}}h_y\delta k = F E_x^2 + G h_y E_x, \quad (\text{A5})$$

where F and G are two constants related to microscopic parameters. From this simple consideration one expects that in the absence of magnetic field the linear anomalous out-of-plane EE vanishes, while it persists as a second-order response in the electric field.

Appendix B: Parameter fit for RuO₂ bilayer

Here we extract the parameter γ of Hamiltonian (1) from DFT data of RuO₂ bilayer. In Fig. 6 we show the DFT data of RuO₂ and the fit of the band structure for the two bands crossed by the Fermi level. We fitted these two bands using the quadratic expression $E_i = a_i k_x^2 +$

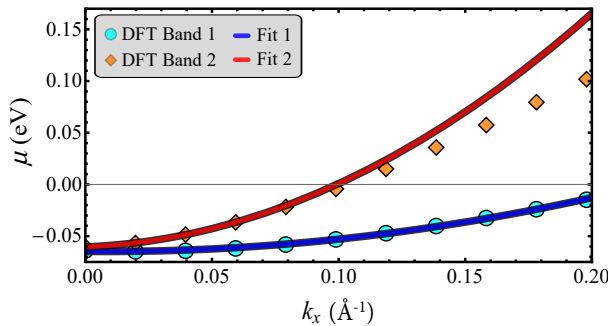


Figure 6. Fit of the bands crossing the Fermi level nearby Γ along the direction ΓY .

$b_i k_x + c_i$, where we truncated the DFT bands in order to minimize vertex location of the two parabolas, therefore by minimizing $\bar{k}_i = |\frac{b_i}{2a_i}|$. We obtain from the fitting procedure

$$\begin{cases} E_- = 1.412 \text{ eV}\text{\AA}^2 k_x^2 - 0.023 \text{ eV}\text{\AA} k_x - 0.065 \text{ eV} \\ E_+ = 5.175 \text{ eV}\text{\AA}^2 k_x^2 + 0.094 \text{ eV}\text{\AA} k_x - 0.060 \text{ eV}. \end{cases} \quad (\text{B1})$$

By comparison with the analytical expression of the eigenvalues of Eq. (1) with $\alpha = 0$, $\mathbf{h} = 0$, and $k_y = 0$, which are

$$E_{\pm} = \left(\frac{1}{2m} \pm \gamma \right) k_x^2, \quad (\text{B2})$$

we obtain the value of γ by the ratio

$$\frac{(a_+ - a_-)}{(a_+ + a_-)} = 2m\gamma = 0.571. \quad (\text{B3})$$

For $m = 1$ we obtain $\gamma \approx 0.3$. In absolute value $m = 0.152 \text{ eV}^{-1}\text{\AA}^{-2}$ (which is $1.2m_e$, where m_e is the electron mass) and $\gamma = 1.881 \text{ eV}\text{\AA}^2$. The sign of γ cannot be determined by band comparison alone, but can be fixed by comparison with the spin patterns throughout the Brillouin zone. From Fig. 7, we see that the lower band along the $Y_0\Gamma$ path is polarized with spin down, indicating that $\gamma > 0$.

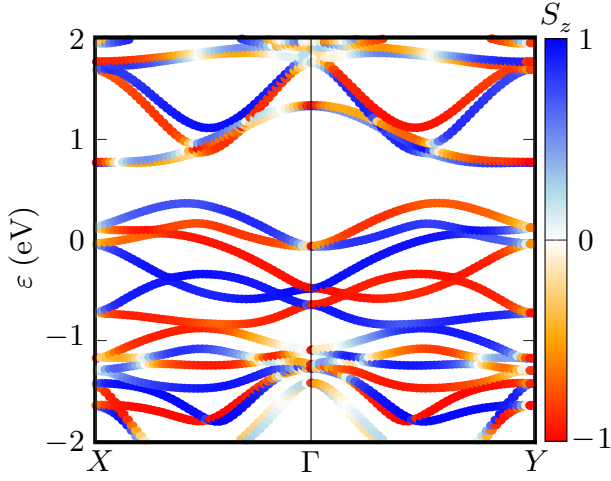


Figure 7. Spin projection along z direction of RuO_2 bilayer.

Appendix C: Behaviour of the response with parameters

This section details the dependence of the Edelstein responses on the RSOC parameter (α) and the Zeeman coupling (h_y). In Fig. 8 we show the in-plane and out-of-plane susceptibility for two values of α . Within this energy window, the response is clearly linear in α . We can understand this result invoking a simple energy scale analysis; the RSOC term is larger than the altermagnetic one for $k \lesssim \alpha/\gamma \sim 10^{-2} \text{ \AA}^{-1}$, and therefore for energies $\varepsilon \lesssim \alpha^2/2m\gamma^2 \sim 10^{-3} \text{ eV}$. On the other hand, below these energies, the dominant energy scale is the weak ferromagnetic coupling h_y . Therefore, across the entire energy range, the RSOC remains a perturbation. The response vanishes for small RSOC.

In Fig. 9, we show the behaviour of the EE for different h_y . The key insight is that the in-plane response is even in h_y , remaining identical for $h_y \rightarrow -h_y$, while the out-of-plane response is odd, changing its sign. Both results are easily understood; the inversion of the magnetic field $h_y \rightarrow -h_y$ can be canceled by a corresponding change in sign $k_x \rightarrow -k_x$, which leaves the eigenvalues of the Hamiltonian unchanged. With such a transformation, the group velocity $v_x \rightarrow -v_x$, and the same goes for the in-plane spin $s_y \rightarrow -s_y$, while the out-of-plane spin, determined by the altermagnetic term, which is even in k_x , remains unchanged $s_z \rightarrow s_z$. Therefore, from the definition of the EE susceptibility, we see that the in-plane response is even, while the out-of-plane response is odd in h_y . Correspondingly, the out-of-plane response, which vanishes for $h_y \rightarrow 0$, must have a linear behavior $\chi_{xz} \propto h_y$ for very small fields. In Fig. 10 we show χ as a function of the Zeeman coupling for a fixed value of the chemical potential $\mu/h_y \gg 1$, in order to show the scaling in the saturation region.

Second-order Edelstein susceptibility— The ratio between of the RSOC and the altermagnetic energy scales is determined by $|\alpha|/|k_F\gamma|$, with k_F to be the Fermi mo-

mentum. It is a measure for their competition, which is strongest when $|\alpha|/|k_F\gamma| \simeq 1$. For the value $|\alpha|/|k_F\gamma| \simeq 1$ we observe that the second-order anomalous susceptibility has a peak. In Fig. 11 we show the second-order anomalous Edelstein susceptibility for different values of γ . It tends to peak at a small value of the chemical potential close to the band crossing at Γ (see Figure 2). The peak is substantially broadened when $|\gamma k_F| > |\alpha|$. Indeed the peak-shape of the second-order response is lost for small values of γ ($\gamma = 0.2 \text{ eV \AA}^2$). Within the considered range of μ values, the maximum explored Fermi momentum corresponds to $k_F = 0.22 \text{ \AA}^{-1}$, so that $|\alpha| > |\gamma k_F|$. However, since the non-relativistic spin splitting is expected to be larger (as seen from DFT calculation), the peak-shape feature might be used as a probe of the band crossing due to the Rashba coupling. To see why the non-monotonicity arises, it is useful to look at the integrand in Eq. (D8) by moving the chemical potential. We show in Fig. 12 the integrand for different chemical potentials, using as benchmark values $\gamma = 1.881 \text{ eV \AA}^2$ and $\alpha = 52 \text{ meV \AA}$. We can see that, as long as the chemical potential is close to the band crossing, the inner band contribution is stronger than the outer one. Moreover, the integrand structure is peaked where the avoided crossings are located. For higher filling the two contributions compensate and the total integral approaches to zero.

In order to quantify the effect of the maximum efficiency of conversion, in Fig. 13(a) we show how the response is behaving by increasing γ at a fixed chemical potential far away from the peaked region, i.e., $\mu = 0.011$ that is the vertical dashed line in Fig. 11, and in Fig. 13(b) the maximum value of the peak for each γ ;

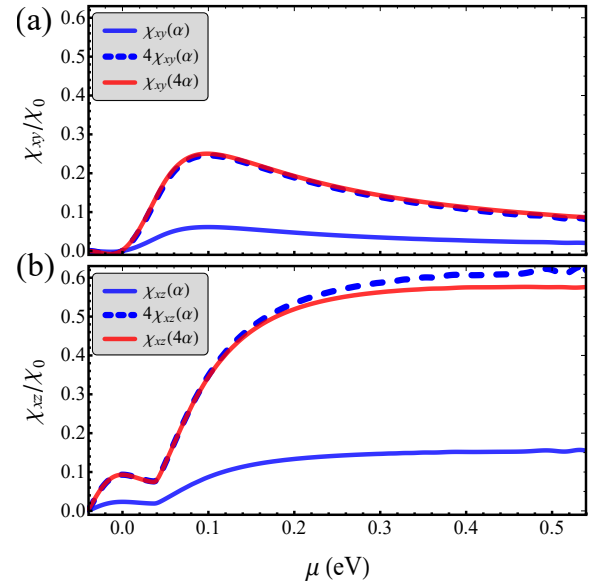


Figure 8. (a) χ_{xy} and (b) χ_{xz} as a function of the chemical potential for $\alpha = 13 \text{ meV \AA}$ and $4\alpha = 52 \text{ meV \AA}$, together with the value of (a) $4\chi_{xy}$ and (b) $4\chi_{xz}$, using $\gamma = 1.881 \text{ eV \AA}^2$, $h_y = 40 \text{ meV}$.

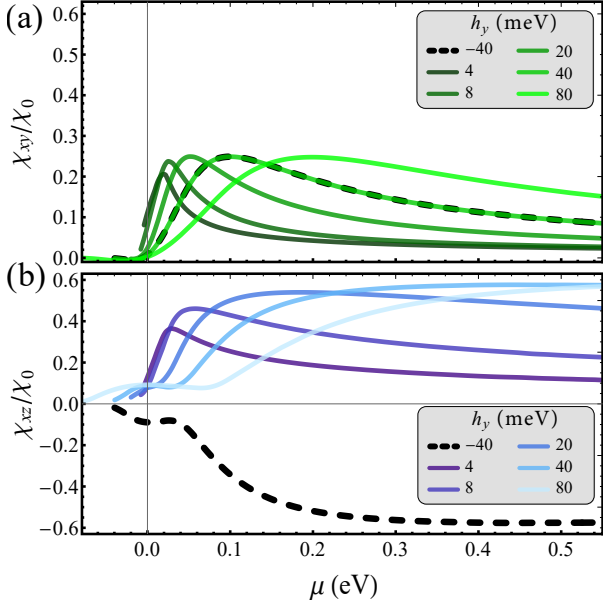


Figure 9. (a) χ_{xy} and (b) χ_{xz} as a function of the chemical potential for $\alpha = 52$ meV \AA and different values of the in-plane Zeeman field h_y .

in both cases we observe a non-monotonic behaviour.

Finally, to quantify the effect of the RSOC, we show in Fig. 14 the dependence on α of the second-order Edelstein susceptibility. As expected from Eq. (A5), for a fixed chemical potential the susceptibility is an even function of α , showing also a sign change for α close to zero.

Appendix D: Boltzmann approach to non-linear EE

Edelstein response up to second order is given by

$$\langle \sigma_k \rangle = \chi_{ik} E_i + \tilde{\chi}_{ijk} E_i E_j, \quad (\text{D1})$$

where $\langle \sigma_k \rangle$ is the magnetization in the k direction, E_i is the i -th component of the electric field, and χ_{ij} is the

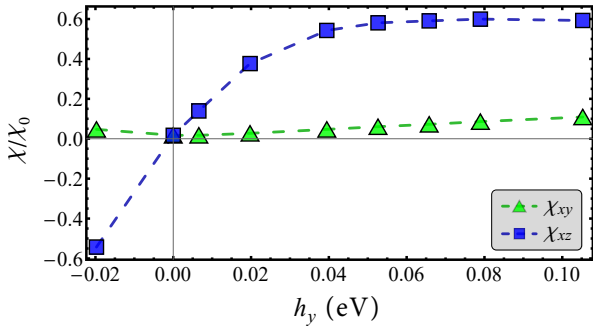


Figure 10. Edelstein susceptibility behaviour with Zeeman coupling for $\alpha = 52$ meV \AA and for fixed chemical potential $\mu = 1.05$ eV and $\gamma = 1.881$ eV \AA^2 . Lines are guides to the eye.

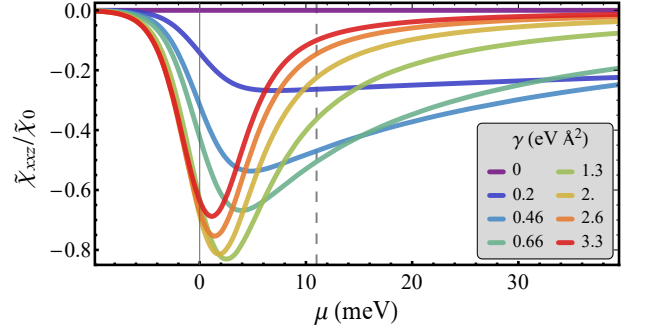


Figure 11. Second order Edelstein susceptibility as a function of the chemical potential for $\alpha = 52$ meV \AA and different values of γ . The dashed vertical line marks the value of μ used for Fig. 13(a).

linear Edelstein susceptibility, while $\tilde{\chi}_{ijk}$ is the second order susceptibility. We can also define the magnetization $\langle \sigma_k \rangle$ also given by

$$\langle \sigma_k \rangle = \mu_b \sum_{n \text{ occ}} \int \frac{d^2 \mathbf{k}}{(2\pi)^2} s_k^n(\mathbf{k}) f(\mathbf{k}), \quad (\text{D2})$$

where s_k^n is the k -th spin component for the n -th band and $f(\mathbf{k})$ is the complete thermal distribution.

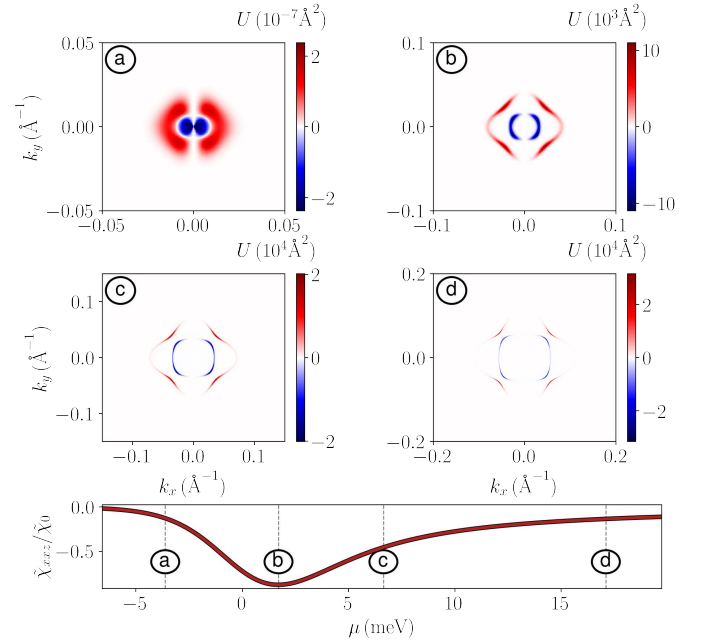


Figure 12. (a-d) Contour plots of the integrand $U = \sum_{\nu} \nu \partial_{k_x} s_z v_x^{\nu} \delta(\epsilon^{\nu} - \mu)$ in Eq. (5) for different values of μ corresponding to the dashed vertical lines of the bottom panel. The benchmark parameters have been chosen as $\gamma = 1.881$ eV \AA^2 and $\alpha = 52$ meV \AA . The Dirac delta function has been substituted with the derivative of the thermal Fermi function, with a temperature of $T = 33$ K, corresponding to $T = 2.8$ meV.

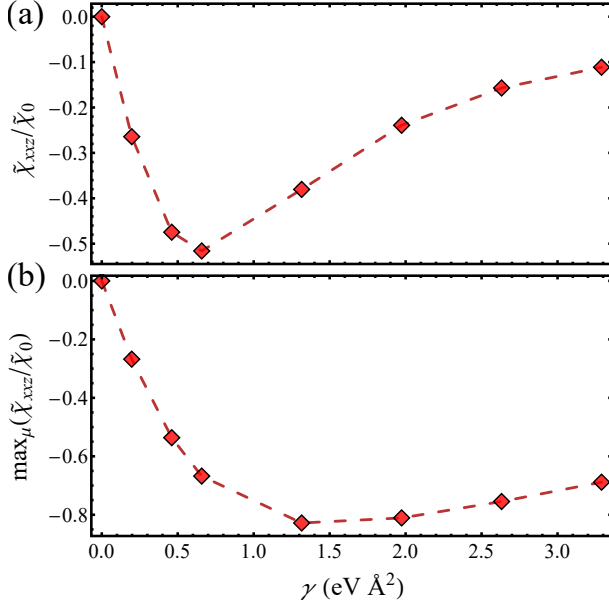


Figure 13. (a) Dependence of the second-order Edelstein susceptibility on the alternating coupling γ (expressed in $\text{eV } \text{\AA}^2$), for $\alpha = 52 \text{ meV } \text{\AA}$ and for fixed chemical potential $\mu = 11 \text{ meV}$, which corresponds to the dashed vertical line in Fig. 11. (b) Maximum of second-order Edelstein susceptibility versus the Zeeman coupling for $\alpha = 52 \text{ meV } \text{\AA}$. Lines are guides to the eye.

In the Boltzmann approach, the equation for the particle distribution f is the following

$$\frac{\partial f}{\partial t} + \frac{d\mathbf{r}}{dt} \cdot \frac{\partial f}{\partial \mathbf{r}} + \frac{d\mathbf{k}}{dt} \cdot \frac{\partial f}{\partial \mathbf{k}} = \text{Coll}, \quad (\text{D3})$$

where $\text{Coll} = -\frac{\varphi}{\tau}$, with τ being the relaxation time that we are considering a constant, $\varphi = f - f_{th}$, and f_{th} the Fermi-Dirac distribution. To first order, for stationary transport and in homogeneous materials, the previous equation becomes

$$-|e|\mathbf{E} \cdot \nabla_{\mathbf{k}} f_{th} = -\frac{\varphi^{(1)}}{\tau}, \quad (\text{D4})$$

where $\varphi^{(1)}$ is the correction to the particle distribution at the first order and e is the electron charge. Solving Eq. (D4) leads to

$$\varphi^{(1)} = |e|\tau \mathbf{E} \cdot \nabla_{\mathbf{k}} f_{th}. \quad (\text{D5})$$

For the next order in the electric field, it is necessary to start again from the Boltzmann equation, which now takes the form

$$-|e|\mathbf{E} \cdot \nabla_{\mathbf{k}} \varphi^{(1)} = -\frac{\varphi^{(2)}}{\tau}, \quad (\text{D6})$$

where $\varphi^{(2)}$ is the the correction to the particle distribution at the second order in the electric field \mathbf{E} . We

neglect the effect of the magnetic field \mathbf{B} since, by considering an in-plane magnetic field in a 2D system, we have $(\mathbf{v} \times \mathbf{B}) \cdot \nabla_{\mathbf{k}} \varphi^{(1)} = 0$.

Substituting Eq. (D5) into Eq. (D6), and considering a constant τ , $\varphi^{(2)}$ can be written as

$$\varphi^{(2)} = e^2 \tau^2 \frac{\partial}{\partial k_j} \left(\frac{\partial f_{th}}{\partial k_i} \right) E_i E_j. \quad (\text{D7})$$

Therefore, we obtain

$$\tilde{\chi}_{xxz} = -\mu_B e^2 \tau^2 S_{\text{cell}} \sum_{\nu} \int \frac{d^2 \mathbf{k}}{4\pi^2} \nu \frac{\partial s_z(\mathbf{k})}{\partial k_x} \delta(\varepsilon_{\mathbf{k}}^{\nu} - \mu) v_x^{\nu}(\mathbf{k}). \quad (\text{D8})$$

We can estimate the coefficient $\tilde{\chi}_0 = \frac{\mu_B e^2 \tau^2}{4\pi^2} S_{\text{cell}}$, with a the characteristic length of our system, which will be the lattice parameter, S_{cell} to be the area of the unit cell, as

$$\tilde{\chi}_0 = 2.36 \times 10^{-14} \frac{\text{m}^2}{\text{V}^2}. \quad (\text{D9})$$

It is straightforward to demonstrate the necessity of the RSOC in order to have a non-vanishing $\tilde{\chi}_{xxz}$. We can consider the integrand of Eq. (D8) without the derivative of the Fermi function as

$$G^{\pm}(k_x, k_y) = \pm v_x^{\pm}(k_x, k_y) \frac{\partial s_z(k_x, k_y)}{\partial k_x}. \quad (\text{D10})$$

The group velocity (corresponding to the system of Eq. (1) for $\alpha = 0$) is

$$v_x^{\pm}(k_x, k_y) = \frac{k_x}{m} \pm 2\gamma k_x \text{sgn}(k_x^2 - k_y^2), \quad (\text{D11})$$

while the spin for the two bands can be written as

$$s_z(k_x, k_y) = \text{sgn}(k_x^2 - k_y^2), \quad (\text{D12})$$

which corresponds to the following derivative

$$\frac{\partial s_z(k_x, k_y)}{\partial k_x} = 4k_x \delta(k_x^2 - k_y^2). \quad (\text{D13})$$

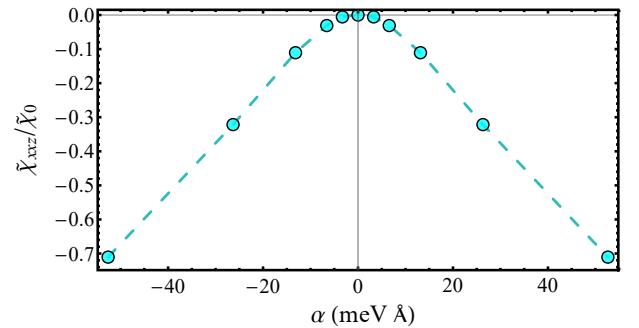


Figure 14. Second-order Edelstein susceptibility $\tilde{\chi}_{xxz}$ as a function of α for $\mu = 0$ and $\gamma = 1.881 \text{ eV } \text{\AA}^2$. The line is a guide to the eye.

The integrand for the two bands is therefore

$$G^\pm(k_x, k_y) = \pm 4k_x^2 \delta(k_x^2 - k_y^2) + 8\gamma k_x^2 \delta(k_x^2 - k_y^2) \text{sgn}(k_x^2 - k_y^2). \quad (\text{D14})$$

The presence of $\delta(k_x^2 - k_y^2)$ makes this integrand non-zero only along the $k_x = \pm k_y$ lines; however, since the full integrand is $\sum_{\pm} G^\pm(k_x, k_y) \delta(\varepsilon^\pm(k_x, k_y) - \mu)$, at fixed μ along these lines only the four points of degeneracy of the two bands contribute to the conductance. Moreover, since they are degenerate, we can write the sum of G^+ and G^- as

$$\mathcal{G} = G^+(k_x, \pm k_x) + G^-(k_x, \pm k_x) = 16\gamma k_x^2 \text{sgn}(k_x^2 - k_x^2). \quad (\text{D15})$$

However, the sign function (sgn) on these lines corresponds to the exact point where the function has a discontinuity. In this case, we can either set $\text{sgn}(0) = 0$, or consider the sum of the left and right limits of the sgn function. In either case, the sum of these points leads to a vanishing the conductance.

Appendix E: Temperature dependence

For higher temperatures, Figure 15 displays $\chi_{xi}(\mu)$ for two different benchmark values. Increasing the temper-

ature from 33 K to 328 K preserves the overall behavior of the susceptibility by changing the chemical potential reported in Fig. 4(c), only smoothing out the curves, especially at low fillings.

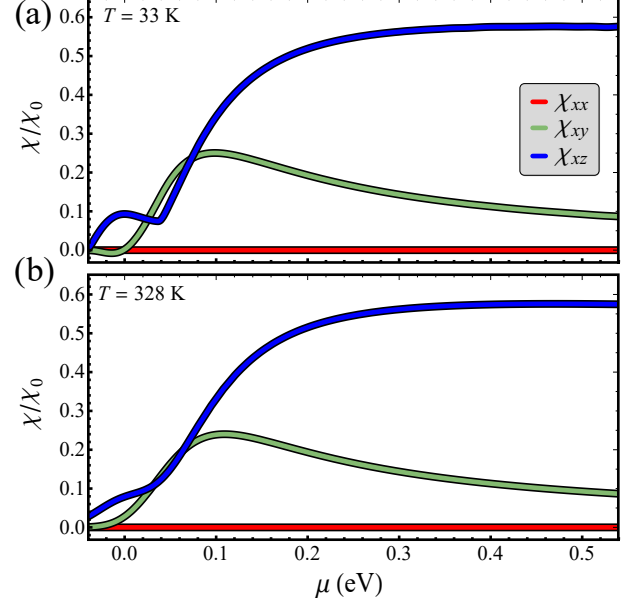


Figure 15. Comparison of the calculated Edelstein susceptibility for $T = 33$ K and $T = 328$ K, considering the parameters $\gamma = 1.881$ eV \AA^2 , $\alpha = 52$ meV \AA , and $h_y = 40$ eV.